Vector-IM-based assessment of alternative framing systems under bi-directional ground-motion

C. Málaga-Chuquitaype [1a], K. Bougatsas[a]

[a]*Department of Civil and Environmental Engineering, Imperial College London, UK*

Abstract

This paper examines the seismic performance of steel buildings with alternative framing systems subjected to bi-directional ground-motion. Peak drifts of one-way (perimeter framing) and two-way (space framing) systems are assessed by means of scalar and vector-valued probabilistic methods. Extensive non-linear response history analyses over idealized 3D structures representing 6- and 9-storey buildings are performed under pairs of linearly scaled ground-motions. Both far-field and near-field non-pulselike acceleration series are considered. The spectral acceleration of the geometric mean of the two horizontal components ($S_{a,GM}$) is taken as the primary intensity measure (IM) while four other ground-motion parameters are employed to construct IM-vectors including: the spectral acceleration ratio (R_{T_3,T_1}), the spectral shape parameter (N_p), and two frequency content parameters (T_m and T_o). This paper shows that incorporating the vector $\langle S_{a,GM}, N_p \rangle$ into the assessment of bi-directionally loaded 3D buildings yields up to 40 % lower conditional standard deviations than a purely scalar formulation at large drift levels while the vector $\langle S_{a,GM}, R_{T_3,T_1} \rangle$ is more efficient at smaller drifts. The effects of alternative framing systems on structural fragilities are found to differ depending on the number of storeys. For 6-storey structures, consistently higher capacities are observed in two-way layouts with respect to one-way systems but they are associated with increasing variabilities at larger demand levels. Conversely, the 9-storey two-way building experiences 5 % lower mean capacities than its one-way counterpart. Finally, drift hazard curves are calculated by combining the building fragilities with idealized ground-motion hazard estimates. The results indicate that one-way buildings experience consistently

[1]Corresponding author: c.malaga@imperial.ac.uk

lower drift exceedance rates regardless of the ground-motion type, especially for drift levels larger than 2 % although the differences are larger for the 9-storey frames in comparison with their 6-storey counterparts. This study represents a first attempt to implement vector-valued analysis in the context of bi-directionally loaded structures and its results constitute an important step towards discerning the most favourable framing system at different seismic performance levels.

Keywords: steel framing systems, bi-directional seismic loads, 3D steel frames, seismic fragilities, performance-based seismic design, vector-valued seismic assessment

---

1. Introduction

Distinct structural systems prevail in different regions of the world depending on the construction skills, history and industrial context of each particular community. This is the case of Japan on the one hand and North America and Europe on the other where two distinguishable steel framing systems have been traditionally employed. Japanese engineers have usually adopted a two-way (space framing) layout consisting of 3D beam-column assemblages designed to resist seismic and gravity loads simultaneously [1]. By contrast, American and European seismic codes differentiate clearly between primary and secondary lateral resisting systems and seek to provide the primary frames with adequate seismic strength and ductility while the secondary, or gravity, frames are designed to resist gravity loads only (e.g. perimeter framing). These secondary frames, which do not contribute significantly in terms of base shear or stiffness at low deformation levels, are known to exhibit large elastic deformation capacities and can enhance the overall post-elastic response of the building if properly designed [2, 3]. Therefore, the question arises as to which of the two building configurations (one-way or two-way frames) has a better performance at different levels of seismic demand.

Likewise, although the importance of considering bi-directional earthquake actions in structural assessments has long been recognised [4, 5] and the torsional response of non-symmetric buildings has been the subject of extensive research [6, 7] including the development of simplified assessment

and modelling procedures [8, 9], comparative studies on the behaviour of different framing systems under bi-directional loads are lacking and no previous study has taken advantage of the benefits brought about by vector-based approaches. Liao et al. [10] developed 3D models of 3-storey Moment Resisting Frame (MRF) buildings with pre and post-Northridge connection details and used them to evaluate the effects of connection fracture, gravity frame contribution and column deformation on the whole building performance. Although not directly addressing the influence of alternative framing systems, this study indicated that pre-Northridge buildings have a much higher probability of failure than the newer designs at all performance levels. Tagawa et al. [1] evaluated the seismic performance of two 3-storey 3D building models with one-way and two-way framing through inelastic dynamic analyses. It was shown that the two-way layout had a smaller mean annual probability of exceedance for inter-storey drifts of less than 3 % whereas larger mean annual probabilities of exceedance were observed for greater drifts. Nevertheless, this study focused only on 3-storey MRFs, used Spectral Acceleration as the single scalar ground-motion intensity measure, and applied single-component recorded acceleration records at 45^o to the building axes. More recently, Erduran and Ryan [11] examined the response of a 3-storey Concentrically-Braced (CB) frame building with varying mass eccentricities under bi-directional loading. Storey drifts from bi-directional excitations were found to be much larger than those resulting from uni-directional earthquake action. Also, it was argued that buildings with CB frames closer to the mass centre may have the potential for significant peak drift reduction but no confirmation of this was offered. However, no study incorporated vector-based approaches for bi-directional shaking and no comparative assessment of the response of multi-storey mid-rise buildings has been offered.

Given the uncertainties involved, the evaluation of the performance of alternative framing systems ought to be carried out within an explicit probabilistic framework, the formalization of which came about one and a half decades ago in the form of guidelines published by the US Federal Emergency Management Agency (FEMA) [12]. Such probabilistic assessment framework can be expressed as:

$$\lambda_{EDP}(x) = \int_{IM} P(EDP > x \mid IM = im) \times |d\lambda_{IM}(im)| \tag{1}$$

where $\lambda_{EDP}(x)$ is the mean annual rate of exceeding a certain value of EDP,

EDP stands for Engineering Demand Parameter and represents the variable under which judgements can be made in terms of structural performance, and IM stands for Intensity Measure and defines the ground-motion intensity at the site under study. In the case of steel MRF, the EDP of choice is customarily the maximum inter-storey drift, θ_{max}, due to the strong correlation between θ_{max} and earthquake damage, while the elastic 5 %-damped Spectral Acceleration at the first structural period, $S_a(T_1)$, is usually taken as the intensity measure thus making IM both site as well as structure specific. Noteworthy, the first term of the product inside the integral in Equation 1 is commonly referred to as the fragility of the structure. It expresses the probability of exceeding the EDP value of interest given that the IM admits a certain value, im. Similarly, the second term inside the integral in Equation 1 is the site hazard (i.e. the mean annual rate of exceeding a value of IM). It should be noted that under this definition, im is a scalar quantity and therefore Equation 1 presupposes that the ground-motion can be well-characterized by a single parameter.

The possible lack of sufficiency of a single intensity parameter to characterize the ground-motion has lead researchers to express the above mentioned probabilistic assessment framework in vector form [13]. The sufficiency of an IM is associated with the degree to which the conditional probability distribution referred to in Equation 1 is independent from other ground-motion parameters. It is an intuitive remark that a complicated phenomenon such as an earthquake ground-motion cannot be be described by a single intensity measure, even if this is structure specific in a particular way. With this purpose, Equation 1 can be reformulated as:

$$\lambda_{EDP}(x) = \int_{IM_1} \int_{IM_2} P(EDP > x \mid IM_1 = im_1, IM_2 = im_2) \times |d\lambda_{IM_1,IM_2}(im_1, im_2)| \tag{2}$$

which involves two Intensity Measures (IM_1 and IM_2). The concept can be extended if more than two intensity measures are considered. By taking into account more ground-motion parameters, improved estimations of structural response are expected which should allow for a better performance assessment. Although vector-valued approaches are conceptually a simple extension of the scalar case, their implementation in practice has not been well established [14] and the identification of a suitable vector of IM remains constrained by the availability of adequate prediction equations and by the

efficiency of their combination [15]. An efficient IM set will allow for a reduced variability in the quantification of the structural response, hence decreasing the standard error on the sample mean of the EDP and potentially cutting down the number of analyses required to achieve a given accuracy in the response estimation. To this end, Faggella et al. [16] performed a probabilistic evaluation of the 3D seismic response of a single reinforced-concrete building and identified the shortcomings of using $S_a(T_1)$ as the only IM. The authors advocated strongly for the use of vector formulations when 3D structures are considered. However, they did not perform a vector-IM-based assessment of probabilistic demands. Similarly, no comparative assessment of the response of multi-storey mid-rise buildings with different framing layouts have been carried out to date. Especially from a vector-valued seismic assessment perspective.

In light of the above discussion, the objective of this paper is twofold: i) first, it seeks to provide a detailed quantification of the benefits of employing a vector-valued analysis over a scalar formulation when evaluating maximum inter-storey drifts in 3D buildings, including an appraisal of the suitability of various vector-IMs for bi-directional seismic actions; and ii) to offer a rigorous comparison of the response of steel buildings with alternative framing configurations by means of vector-valued probabilistic evaluations. To this end, four vector-IMs related to the ground-motion frequency content and spectral shape are studied. First, the one-way and two-way structures under consideration and their corresponding finite element models are presented followed by the ground-motion dataset considered. Practical aspects related to the bi-directional loading and parameter definition are then introduced and fragility curves as well as fragility surfaces are defined by means of scalar and vector formulations, respectively. The application of the probabilistic framework to the estimation of drift hazard curves is also presented. This study constitutes the first attempt to implement a vector-based comparison of the world's two most prevailing steel framing systems when subjected to realistic bi-directional earthquake action. The results presented herein represent an important step towards identifying the steel framing layout with the most favourable seismic performance at different demand levels.

2. Structural systems and earthquake ground-motions

This section describes the buildings under study as well as the simplified numerical models employed to represent them. Structures of 6 and 9 storeys with one-way and two-way framing systems are examined. The main characteristics of the ground-motion datasets used, including far-field as well as non pulselike near-field records, are also introduced below.

2.1. Framing systems

Figure 1 presents the layout of the two main framing systems examined in this study, namely: one-way and two-way frames. As noted above, two-way buildings are designed such that all structural elements resist lateral loads. On the other hand, a few selected frames (usually towards the building perimeter) are designed to sustain the entirety of lateral actions in one-way buildings while the other frames are assumed to carry gravity loads only. Symmetric five bay-by-five bay layouts with 5-metre bays and 5 % mass-eccentricity are examined. It is believed that these can offer an insight into the general behavioural trends of the two building systems analysed and provide a good basis for future studies incorporating a wider range of geometric variations. Besides, the symmetric nature of the frames under study facilitates the analysis of the extent to which different vectors of IM influence the response estimation. The storey height is kept constant at 3 m while 6-storey and 9-storey buildings are considered making a total of 4 structures. The 6-storey and 9-storey structures were designed to resist a total base shear of 13 and 10 % their weight, respectively. As noted before the design of one-way buildings disregarded the stiffness and strength contribution of secondary systems in accordance with common practice in such cases. W14x38 and W12x35 beams were employed for the lower 4 and upper 2 storeys in 6-storey buildings, respectively. Similarly, W14x38 to W14x30 sections were used for the 9-storey building. Square hollow sections ranging between 400x400x16 mm and 300x300x12.5 mm were employed for the columns in two-way frames while HEB400 to HEB320 column sections were used in one-way buildings. More specific details of the frames can be found elsewhere [17, 18]. The main structural characteristics of the frames are summarized in Table 1 where T_1 stands for the period of the first vibration mode while V_y/W_{tot} is the yield strength normalized over the total building weight as obtained from a static non-linear analysis with a constant first mode lateral loading profile along the height of the building.

The onerous computational demands associated with bi-directional response-history analyses are alleviated herein by employing equivalent fish-bone models of reduced number of degrees of freedom to represent the buildings as schematically depicted in Figure 2. In the case of one-way structures (Figure 2b), the lateral resisting frames acting primarily in-plane are simulated by four primary frames with pin-ended beams fully fixed to the columns. In turn, all the gravity frames are summed up in a single continuous column connected to the other frames by means of rigid diaphragm constraints. On the other hand, the two-way framed buildings (Figure 2a) are modelled with four columns and fully fixed beam-to-column connections at both beam ends. The adequacy of these simplified models to estimate peak deformations of multi-storey buildings, including bi-directionally loaded ones, has been extensively established in previous studies [17, 19, 20]. Fibre-based FE models were constructed in OpenSees [21] accounting for material and geometric non-linearities. Force-based elements with at least 60 sectional fibres were employed to represent all structural elements, including the gravity frames. A corotational geometric transformation was utilized and a superimposed load of 3000 N/m^2 was assumed for all storeys. In addition, a Bilinear steel material model was considered with an Elastic Modulus of 210 GPa and 3 % post-elastic strain hardening. This value of material strain hardening was assumed based on typical modelling practice [22, 23]. It is worth noting however that the use of values between 0 and 0.5 % are not expected to have a notable influence in the response for the range of displacement demands of interest for the present study, where collapse prediction is not the focus, as illustrated by [24, 25]. The FE models employed and their fundamental modes are depicted in Figure 3.

2.2. Ground-motion records

The two sets of acceleration series suggested by the Federal Emergency Management Agency [26] were employed herein including far-field and near-field non-pulselike records. All 14 pairs of records in the near-field category with no pulses as proposed in [26] were considered as well as the first 16 record pairs with the largest geometric mean peak ground accelerations (PGA_{GM}) form the far-field set. The original unscaled series available in the NGA-West2 database [27] were employed. Since this work is concerned with bi-directional analyses, the axis orientation of the horizontal acceleration components was randomized following the findings of Beyer and Bommer

[28] who noted that the response to horizontal ground-motion components with randomly oriented axes can be used for the estimation of unbiased median EDP responses. This is of particular importance for the near-field pairs which were consistently reported in the fault-parallel and fault-normal directions in their original form [26, 27]. Therefore, new pairs of horizontal acceleration components were defined in this study according to:

$$\begin{pmatrix} a_{x(\alpha)}(t) \\ a_{y(\alpha)}(t) \end{pmatrix} = \begin{bmatrix} cos(\alpha) & sin(\alpha) \\ -sin(\alpha) & cos(\alpha) \end{bmatrix} \begin{pmatrix} a_x(t) \\ a_y(t) \end{pmatrix} \quad (3)$$

where α is the randomized angle of rotation, $a_x(t)$ and $a_y(t)$ are the original ground-motion horizontal components in x and y directions, respectively, and $a_{x(\alpha)}(t)$ and $a_{y(\alpha)}(t)$ are the obtained rotated components. Table 2 summarizes the catalogue of earthquakes employed including their Moment Magnitude (M_w), PGA, and α, while their corresponding spectra are presented in Figure 4.

3. Non-linear response history analyses and intensity measures

A series of non-linear response history analyses were performed on the FE models described above by linearly scaling each pair of ground-motion records to pre-defined levels of intensity. The hunt and fill algorithm proposed by Vamvatsikos and Cornell [29, 30] was applied to this effect while spline interpolation was used to obtain continuous IM versus EDP relationships [30]. Since this paper is concerned with the bi-directional response of 3D models, ground-motion scaling was performed on the spectral acceleration of the geometric mean of the two horizontal components, $S_{a,GM}$ [28]. This is particularly relevant to the structures considered here since they are symmetric (i.e. $T_1 \approx T_2$). Besides, $S_{a,GM}$ is directly applicable for coupling fragility analysis with hazard estimates [31]. Similarly, the absolute maximum inter-storey drift in any direction along the height of the building, θ_{max}, was taken as the EDP. Also, since the interest of this study is on the slight to extensive damage states that tend to dominate loss estimates rather than on collapse prediction, a target maximum drift of $\theta_{max} = 7$ % was employed to set the limits of analysis. As noted by [32], care should be taken when utilizing linearly scaled ground-motion records within a vector-IM based framework. This is due to the fact that different intensity measures scale differently for the same scaling level. However, ground-motion scaling was

considered adequate for the present study since its main interest lies in the identification of behavioural trends for which the preservation of the natural correlations between IMs is not of primary importance. Furthermore, none of the secondary IM employed scales with spectral ordinates and therefore consistency is maintained among all parameter combinations studied.

From a structural engineer's perspective, the selection of a second intensity measure (IM_2 in Equation 2) should be such that the requirements for more demanding calculations are balanced by an improvement in the explanation of the structural response. To this end, besides the spectral acceleration $S_{a,GM}(T_1)$, four additional ground-motion parameters were employed to construct vectors of IM, including:

- the *spectral acceleration ratio,* R_{T_3,T_1}, which is the ratio between the spectral accelerations at the third and first structural periods ($S_{a,GM}(T_3)$ and $S_{a,GM}(T_1)$), respectively. Given the symmetric nature of the buildings analysed where $T_1 \approx T_2$, the third period was selected in order to consider the effects of higher modes in the structural response while keeping the estimate of R_{T_3,T_1} stable.

- the *spectral shape parameter,* N_p. This parameter was proposed by Bojórquez and Iervolino [33] and was defined as the average of unidirectional spectral ordinates normalized by $S_a(T_1)$. The efficiency of the vector $\langle IM_1, IM_2 \rangle = \langle S_a, N_p \rangle$ has been proved for planar structures [33]. In the present study, this parameter is extended to bi-directional ground-motion by operating over the geometric mean of the two horizontal components such that:

$$N_p = \frac{S_{a,avg}(T_1 ... T_N)}{S_{a,GM}(T_1)} = \frac{\left(\prod_{i=1}^{N} S_{a,GM}(T_i)\right)^{1/N}}{S_{a,GM}(T_1)} \tag{4}$$

  where T_N is a period that defines the portion of the spectrum to the right of the elastic period that is considered for the characterization of the ground-motion. It follows that N_p aims to incorporate the effects of inelastic periods in the ground-motion characterization. A value of $T_N = 2T_1$ and a step of ΔT_i=0.001 second was used herein which enabled stable estimates of N_p to be made. Although ground-motion models do not currently exist to predict N_p, they can be obtained

on the basis of a prediction equation for spectral accelerations and a correlation model for different spectral ordinates. Th formulation of one of such models is shown later in this paper.

- finally *the frequency content parameters, T_m and T_0*, were also included in the seismic assessment. Importantly, ground-motion prediction equations have already been developed for the estimation of T_m and T_0 [34]. Also, the *Mean Period*, T_m of the ground-motion has been previously found to improve the estimation of peak displacements in steel structures [35, 36] subjected to one-directional loading. T_m is calculated by weighting the amplitudes of the Fourier Spectrum as follows:

$$T_m = \frac{\sum_i \beta_i^2 \frac{1}{f_i}}{\sum_i \beta_i^2}, \text{ for } 0.25 \text{ Hz} \leq f_i \leq 20 \text{ Hz} \tag{5}$$

where β_i is the Fourier Amplitude Coefficient at frequency f_i. A minimum frequency step of $\Delta f \leq 0.05$ Hz is used for the Fourier Transform in order to get a stable representation of its frequency content as recommended in [37]. Additionally, the *Smoothed Predominant Period*, T_o, which is based on the 5 %-damped elastic response spectrum rather than the Fourier spectrum was also evaluated. T_o is defined as:

$$T_o = \frac{\sum_i T_i \cdot \ln\left(\frac{S_a(T_i)}{PGA}\right)}{\sum_i \ln\left(\frac{S_a(T_i)}{PGA}\right)}, \text{for } T_i \text{ with } \frac{S_a}{PGA} \geq 1.2, \; \Delta \log T_i \leq 0.02 \tag{6}$$

Therefore, only the periods for which $S_a \geq 1.2$ PGA are considered in the calculation of T_0 while equal spacing is adopted in the logarithmic space. As a result, T_o is more representative of the the high to moderate frequencies in the spectrum.

It is important to note that the calculation of all ground-motion parameters have to be carried out in consistency with the bi-directional nature of the analyses carried out in this study. To this end, the Fourier amplitude coefficients in equation 5 were combined by means of the Euclidean

norm [34] when calculating T_m while a Geometric Mean spectrum was used for the computation of T_o, N_p and R_{T_1,T_1}.

Extensive analyses were performed by subjecting the 3D FE models described above to the two sets of ground-motion pairs previously introduced. Linear ground-motion scaling was applied as outlined in the previous section and the corresponding peak deformations were recorded. The data gathered forms the basis for the statistical analyses that follow. The estimation of fractile capacity relationships for the four models under study at different damage states and considering both scalar as well as vector intensity measures for one-way and two-way frames is presented below.

4. Fragility estimations

Probabilistic seismic demand assessment is centred around the estimation of mean annual rates of exceedance of certain EDP levels according to Equations 1 and 2. This section deals with the first multiplication terms inside the integrals of Equations 1 and 2 that express the probability of exceeding a given value of EDP conditional on the intensity of the ground-motion. This function corresponds to a fragility curve if a scalar IM is employed and to a fragility surface if a IM-vector is used.

4.1. Scalar-based fragility curves

When the distribution of the EDP is assumed to be conditional on a single ground-motion characteristic, a scalar IM can be considered and the complementary cumulative distribution function, which defines the probability $P(EDP > x \mid IM = im)$, can be estimated directly. Previous statistical analyses have proven the log-normality of fragility curves [38]. Hence, a log-normal distribution of IM conditional on a given level of EDP can be fitted to the numerical data [39]. The cumulative distribution function, $P(IM < im \mid EDP = x)$, is then used as the fragility function. The method of moments was applied herein in order to estimate the log-normal distribution median, μ_{lnIM}, and standard deviation, σ_{lnIM} [40] for a set of N records where $lnIM_i$ is the i-th capacity value. This procedure is illustrated in Figure 5 for a limit state defined by $\theta_{max} = 0.05$ and for the four structures examined in this study.

Tables 3 and 4 summarize the median capacities and their associated dispersion values for far-field and near-field records, respectively. Three limit states associated with slight, moderate and severe damage, namely $\theta_{max} = \{0.007, 0, 025, 0.05\}$, are reported. It can be observed from Tables 3 and 4 that, in general, a smaller dispersion is associated with the response of 6-storey buildings in comparison with 9-storey ones. This can in principle be explained by the effects of higher modes which increase with structural height. However, for larger drift demands, a significant portion of this variability should also be attributed to inelastic period lengthening as will be argued later with reference to the incorporation of N_p in an IM-vector. Finally, the efficiency of the scalar intensity measure (quantified herein by σ_{lnIM}) decreases significantly as the drift limit increases. This is a direct consequence of the larger levels of inelastic excursions at higher drifts for which the first elastic period becomes less relevant. The same observations hold true also for the case of near-fault records (Table 4).

4.2. Vector-valued fragility surfaces

The proven lack of sufficiency associated with scalar IMs can lead to erroneous and biased results, especially in the case of 3D analysis. In order to avoid these shortcomings and quantify their effects, this section presents the statistical modelling assumptions adopted for the definition of vector-valued fragility surfaces. It starts with a preliminary comparison of current modelling alternatives and leads to the comparative assessment of the efficiency of alternative intensity measures presented later in the paper.

In total, three different statistical modelling approaches were evaluated in terms of their applicability to the estimation of fragility surfaces of bi-directionally excited 3D buildings. Firstly, the Logistic Regression initially proposed by Shome and Cornell [41] was considered. This method was originally used to characterise the collapse and non-collapse response and was later employed by Bojórquez et al. [42] to estimate fragilities by treating $(EDP > x)$ as a binary variable. To this end, a binary response can be inferred by regressing on the known binary outcomes at each $S_{a,GM}(T_1)$ level of interest. Hence, the probability of failure can be expressed as:

$$P(fail \mid S_{a,GM}(T_1) = s_{a,GM}, IM_2 = im_2) = \frac{1}{1 + e^{-(b_0 + b_1 \cdot im_2)}} \qquad (7)$$

where the coefficients b_0 and b_1 are estimated by means of logistic regression [43] while the probability of exceeding a certain value of EDP for the non-failure data is calculated using linear regression. Severe inconsistencies arose between results at successive $S_{a,GM}$ levels when the method was applied to the dataset generated in this study. These anomalies might have been caused by the effects of scaling and spline interpolation [30] or the number of record pairs employed.

Subsequently, the Improved Logistic Regression methodology proposed by Bojórquez et al. [42] was also evaluated. To this end, regressions were performed utilizing both primary and secondary intensity measures as estimators such that:

$$P(fail \mid S_{a,GM}(T_1) = s_{a,GM}, IM_2 = im_2) = \frac{1}{1 + e^{-(b_0 + b_1 \cdot s_{a,GM} + b_2 \cdot im_2)}} \quad (8)$$

where the coefficients b_0, b_1 and b_2 are calculated using logistic regression on the whole dataset. Figure 6 illustrates the application of multiple logistic regression to the 6-storey two-way frame using R_{T_3,T_1} as secondary intensity measure. It can be appreciated from this figure that the values of $P(EDP > x \mid S_{a,GM}(T_1) = s_{a,GM_1}, IM_2 = im_2)$ are non zero for $S_{a,GM}(T_1) = 0$. This has important implications for the estimation of drift hazard curves since coupling conservative values of fragility at low levels of IM with the corresponding high ground-motion hazard at those levels can lead to significant overestimations of $\lambda_{EDP}(x)$. Similar issues have been identified by Gehl et al. [14] while using linear regression procedures, instead of logistic regression, for the response evaluation of planar unreinforced masonry structures.

Finally, linear regression which can be considered as an extension of scalar fragility fitting [39], was adopted. In this case, the probability of exceeding an EDP value is given by:

$$P(EDP > x \mid S_{a,GM} = s_a, IM_2 = im_2) = \Phi\left(\frac{ln(s_{a,GM}) - (b_0 + b_1 \times ln(im_2))}{\hat{\sigma}_{cap}}\right) \quad (9)$$

where b_i are regression coefficients, $\hat{\sigma}_{cap}$ is the standard error of the residuals and Φ is the cumulative density function of the distribution. Figure

7 presents a fragility surface obtained by means of linear regression for the 6-storey two-way frame considering N_p as secondary intensity measure while Figure 8 presents similar results for R_{T_3,T_1} and $S_{a,GM}(T_3)$. The corresponding linear regression fitting is also shown in Figure 8. The coefficient of determination R^2 is included as a goodness of fit measure. The results are also summarized in Table 5. Additionally, the p-value of the b_1 coefficient defined as the T-statistic of the null hypothesis for the statistical significance of b_1 (i.e. b_1=0) is also reported. A small value of p implies the statistical significance of the second IM [44].

It should be noted that problems may arise when implementing linear regression with vectors incorporating strongly correlated IMs. The case of $S_{a,GM}(T_3)$ is presented in Figures 8c and 8d as an example. It can be seen from these figures that the positive correlation between IM_1 and IM_2 has led to very high values of $P(EDP > x)$ at low $S_{a,GM}(T_1)$ levels which can be unsuitable for coupling fragilities and hazard estimations. Similar problems have been reported in [14] when a linear combination of S_{aT_1} and S_{aT_2} was used as a scalar IM. On the other hand, the dimensionless ratio R_{T_3,T_1} computed from the geometric mean spectrum is shown to produce better results in Figure 8a.

5. Simplified drift hazard estimations

The differences in seismic behaviour associated with alternative framing systems, including the effects of σ_{lnIM} on $P(EDP > x)$, can be further examined by comparing their responses in terms of drift hazard curves. To this end, the fragilities calculated above should be combined with ground-motion hazard estimates so as to obtain mean annual rates of exceedance of EDP levels. This section outlines the procedure followed in order to obtain the drift hazard curves employed for comparison purposed. To this end, simplified seismic scenarios associated with punctual sources located at 16 and 4 km from the building site in consistency with the far-field and near-field assumptions, respectively, are utilized. It is fully recognized that simplifying the seismic hazard to a point source is not necessarily comparable with a real Probabilistic Seismic Hazard Assessment for which several sources are usually considered. Despite these simplifying assumptions, important general tendencies can be identified from these analyses as will be discussed

in the following sections. In what follows, attention is given to the scalar $IM_1 = S_{a,GM}$ and the vector $\langle IM_1, IM_2 \rangle = \langle S_{a,GM}, N_p \rangle$ for brevity.

In light of the single distance assumption, the Marginal Moment Distribution can be taken as the joint distribution of magnitude and distance. To this end, a doubly-bounded Gutenberg-Richter exponential distribution with $b = 1.0$ was assumed:

$$F_M(m) = \frac{1 - e^{-\beta(m - m_{min})}}{1 - e^{-\beta(m_{max} - m_{min})}} \tag{10}$$

where $\beta = ln(10) \cdot b$, and $m_{min} = 5$ and $m_{max} = 7$ are the minimum and maximum Moment values that the source can produce, respectively. The Boore and Atkinson [45] ground-motion prediction model was used herein in light of its simplicity.

The second term in Equations 1 and 2 is known as the mean rate density (MRD) [13]. Assuming a discretized moment distribution, this MRD can be estimated as:

$$MRD_{IM}(im) = \nu_{tot} \left\{ \sum_{M} f_{IM}\left(im \mid m, r\right) P_M\left(m\right) \right\} \tag{11}$$

where $f_{IM}\left(im \mid m, r\right)$ is the probability density function of the scalar intensity measure given an earthquake scenario of known magnitude, m, and distance, r.

In the case of a vector-IM formulation, the MRD is defined as:

$$MRD_{IM_1,IM_2}(im_1, im_2) = \sum_{i=1}^{N} \nu_i \left\{ \int_R \int_M f_{IM_1,IM_2}\left(im_1, im_2 \mid m, r\right) f_{M,R}\left(m, r\right) dmdr \right\}_i \tag{12}$$

In contrast with Equation 11, Equation 12 now requires the specification of a joint distribution of IMs given an earthquake scenario of the form:

$$f_{IM_1,IM_2}\left(im_1, im_2 \mid m, r\right) \tag{13}$$

This distribution can be decomposed into the product of a marginal distribution of IM_1, as defined in Equation 2, and a conditional distribution of

IM_2 conditional on IM_1. Assuming log-normality, this conditional distribution can be represented by:

$$\mu_{lnIM_2|im_1,m,r} = \mu_{lnIM_2|m,r} + \rho_{IM_1,IM_2}\frac{\sigma_{lnIM_2|m,r}}{\sigma_{lnIM_1|m,r}}\left(lnim_1 - \mu_{lnIM_1|m,r}\right) \quad (14)$$

$$\sigma_{lnIM_2|im_1,m,r} = \sigma_{lnIM_2|m,r}\sqrt{1-\rho^2{}_{IM_1,IM_2}} \quad (15)$$

where $\mu_{lnIM_2|m,r}$ and $\sigma_{lnIM_2|m,r}$ are the logarithmic mean and standard deviation of the marginal distribution of IM_2, respectively and ρ_{IM_1,IM_2} is the correlation between the two IMs. If N_p is considered as secondary intensity measure, these parameters can be obtained as follows. First, taking the logarithm of Equation 4 we get:

$$lnN_p = \frac{1}{N}\sum_{i=1}^{N} lnS_{a,GM}(T_i) - lnS_{a,GM}(T1) \quad (16)$$

Subsequently, the logarithmic mean and variance of the marginal distribution of lnN_p can be calculated as:

$$\mu_{lnN_p} = \frac{1}{N}\sum_{i=1}^{N} \mu_{lnS_{a,GM}(T_i)} - \mu_{lnS_{a,GM}(T_1)} \quad (17)$$

$$\begin{aligned} Var[lnN_p] = {} & Var[lnS_{a,GM,avg}(T_1...T_2)] + Var[lnS_{a,GM}(T_1)] \\ & - 2\rho_{ln[S_{a,GM,avg}(T_1...T_N)],ln[S_{a,GM}(T_1)]}\sigma_{ln[S_{a,GM,avg}(T_1...T_N)]}\sigma_{ln[S_{a,GM}(T_1)]} \end{aligned} \quad (18)$$

where

$$\begin{aligned} & Var\left\{ln[S_{a,GM,avg}(T_1...T_N)\right\} = \\ & \frac{1}{N^2}\sum_{i=1}^{N}\sum_{j=1}^{N} \rho_{ln[S_{a,GM}(T_i],ln[S_{a,GM}(T_j)]}\sigma_{ln[S_{a,GM}(T_i)]}\sigma_{ln[S_{a,GM}(T_j)]} \end{aligned} \quad (19)$$

and

$$\rho_{ln[S_{a,GM,avg}(T_1...T_N)],ln[S_{a,GM}(T_1)]} = \frac{\sum_{i=1}^{N} \rho_{ln[S_{a,GM}(T_i],ln[S_{a,GM}(T_1)]} \sigma_{ln[S_{a,GM}(T_i)]}}{\sqrt{\sum_{i=1}^{N} \sum_{j=1}^{N} \rho_{ln[S_{a,GM}(T_i],ln[S_{a,GM}(T_j)]} \sigma_{ln[S_{a,GM}(T_i)]} \sigma_{ln[S_{a,GM}(T_j)]}}} \quad (20)$$

Equation 20 was first deduced in [46] and was recapitulated in [33] to be used in conjunction with Inoue and Cornell's correlation relationship between spectral ordinates at different periods [47]. In the present study, the correlation model proposed by Baker and Jayaram [48] was used for the correlation between two spectral acceleration values in Equation 20. The applicability of this correlation model for the geometric mean of two horizontal components has been documented in [49].

In the original study [33], N_p was employed within a seismic hazard assessment framework based on a log-normally distributed hybrid scalar intensity measure IN_p instead of performing a full vector-valued probabilistic seismic hazard analysis. IN_p was defined in [33] as a linear combination of the logarithm of N_p and $S_a(T_1)$:

$$ln(IN_p) = ln(S_a(T_1)) + \alpha \cdot ln(N_p) \quad (21)$$

Such intensity measure emerges from Equation 9 where α corresponds to $-b_1$ and the mean and standard deviation of the logarithm are the intercept (b_0) of the linear regression and the standard error of the residuals (σ_{cap}). However, the use of such intensity measure would require the site seismic hazard to be defined as a function of the parameter α and is therefore dependent on the fragility of the structure. In the present study, in order to allow for a site seismic hazard for the vector-IM, a direct correlation function between $lnSa(T_1)$ and $lnNp$ was sought such that:

$$\begin{aligned} COV\left[lnN_p, lnS_{a,GM}(T_1)\right] &= COV\left[lnS_{a,GM,avg}(T_1...T_N) - lnS_{a,GM}(T_1), lnS_{a,GM}(T_1)\right] \\ &= COV\left[lnS_{a,GM,avg}(T_1...T_N), lnS_{a,GM}(T_1)\right] - COV\left[lnS_{a,GM}(T_1), lnS_{a,GM}(T_1)\right] \end{aligned} \quad (22)$$

$$\Leftrightarrow \rho_{lnN_p,ln[S_{a,GM}(T_1)]} =$$

$$\frac{\rho_{ln[S_{a,GM,avg}(T_1...T_N)],ln[S_{a,GM}(T_1)]}\sigma_{ln[S_{a,GM,avg}(T_1...T_N)]}\sigma_{ln[S_{a,GM}(T_1)]} - \sigma^2{}_{ln[S_{a,GM}(T_1)]}}{\sigma_{lnN_p}\sigma_{ln[S_{a,GM}(T_1)]}} \tag{23}$$

It should be noted that in the case of a vector of the form $\langle IM_1, IM_2 \rangle = \langle S_{a,GM}(T_1), R_{T_3,T_1} \rangle$, the joint hazard is a simplified version of the above formulation since R_{T_1,T_3} can be thought as a rendition of N_p with the nominator consisting of a single value of S_a rather than a geometric mean of multiple values.

6. Comparison between scalar and vector formulations

This section compares the scalar versus vector performance assessments of the buildings under consideration. The comparison is firstly done in terms of scalar and vector fragilities. This is followed by an analysis of their implications on drift hazard estimations. The results presented in this section will be used in latter parts of this paper to evaluate the relative performance of alternative building configurations.

6.1. Fragility functions

Fragility surfaces were calculated by means of linear regression for all structures considered and all IM combinations taking $S_{a,GM}(T_1)$ as the primary intensity measure. The results of these regression analyses are summarized in Tables 5 and 6 for far-field and near-field record datasets, respectively. In addition, Figures 9 to 11 present representative fragility curves conditioned on the minimum and maximum values of IM_2 within the corresponding record set. The values of the slope of the linear regression (b_1) are provided in Tables 5 and 6 along with their p-value, the goodness of fit measure (R^2) and the conditional standard deviation ($\hat{\sigma}_{cap}$).

Performing vector-valued fragility analyses with the *smoothed predominant period*, T_o, as the secondary intensity measure was found to provide no added benefit over a pure scalar calculation. This can be observed from Tables 5 and 6 where high p-values are associated with T_o for all framing configurations. By and large, very little further explanation of the structural

response is provided by T_o since the fragility surfaces were conditional almost exclusively on $S_{a,GM}(T_1)$ when $\langle S_{a,GM}, T_o \rangle$ was used.

On the other hand, including the *mean period*, T_m (calculated from the Euclidean norm of the Fourier spectra of the two ground-motion components) in the IM vector leads to a moderate improvement of the fragility estimations at lower drifts for the 9-storey building and under far-field ground-motions only. In this case, the p-values at the $\theta_{max} = 0.007$ limit are 0.106 and 0.136 for two-way and one-way frames, respectively while a reduction of around 5 % in the dispersion is brought about by including T_m in the vector of IMs. This can be verified by comparing the corresponding values of standard deviation reported in Tables 3 and 5. Figure 9 presents the scalar fragility along with additional fragilities conditional on T_m evaluated at the maximum and minimum T_m values from the record set employed. The reduction in the ability of T_m to express additional information at larger drift levels is evident from the closeness of the fragility curves observed in Figure 9c at $\theta_{max} = 0.025$ relative to those presented in Figure 9a at $\theta_{max} = 0.007$. Also, a minor tendency of T_m to be more efficient for the 9-storey two-way frame than for the 9-storey one-way structure can be observed from Table 5 and Figures 9b and 9d. Furthermore, the mild benefits described above for the vector $\langle S_{a,GM}(T_1), T_m \rangle$ are absent when near-field earthquakes are employed.

The *spectral ratio*, R_{T_3,T_1}, as obtained from the geometric mean spectrum was found useful at lower drift limits ($\theta_{max} = 0.007$) for all the structures considered under far-field records. p-values smaller than 0.05 were found in all cases except for the 6-storey one-way building for which a p-value of 0.16 was observed. Even then, this p-value is the smallest of all secondary IMs examined at this level of deformation (i.e. $\theta_{max} = 0.007$). The ability of R_{T_3,T_1} to provide additional explanation of the structural response diminishes with increasing drift values. This is a direct consequence of the higher mode dependence of the response at small θ_{max} values which period range is well characterized by R_{T_3,T_1}. As the deformation increases, plastic behaviour introduces increasing levels of period lengthening, hence altering the range of periods governing the structural response. When Tables 3 and 5 are compared at the $\theta_{max} = 0.007$ limit state, the use of the vector $\langle S_{a,GM}, R_{T_3,T_1} \rangle$ results in reductions in the associated standard deviations of over 10 % in all structures considered with the exception of the 6-storey one-way building where a 5 % reduction is observed. Figure 10 presents the comparison of

vector and scalar fragilities associated with $\theta_{max} = 0.007$ for far-field earthquakes. Table 5 also shows that approximately 25 % of the variance of the scalar IM can be explained by the secondary IM (i.e. $R^2 \approx 0.25$ for R_{T_3,T_1}) In contrast, when near-field responses are considered (Table 6), the inclusion of R_{T_3,T_1} as secondary IM seems to bring very little benefit for all 3D building configurations examined.

A more favourable performance is observed for the *spectral shape parameter*, N_p, obtained from the geometric mean spectrum, at larger deformations. It can be concluded from the results reported in Tables 5 and 6 that all fragility estimations at large peak drifts (i.e. $\theta_{max} = 0.05$) are affected significantly by the consideration of N_p as a secondary IM. This is true regardless of the framing system under consideration and holds for both far-field and near-field ground-motion sets, although lower improvements are evident for near-field relative to far-field records. On the other hand, the statistical significance of N_p is rather small for lower levels of peak drift. Very small p-values are obtained in all $\theta_{max} = 0.05$ cases with reductions in the corresponding standard deviation of up to 40 % in the case of 9-storey buildings (both one-way and two-way) subjected to far-field acceleration series when compared with the scalar case (Table 5). However, smaller reductions of standard deviation, in the order of 20 %, are observed for 6-storey structures. In the case of near-field actions these reductions are 30 % and 10 % for 9 and 6-storey buildings, respectively. Additionally, with reference to the R^2 values in Table 5, it should be noted that around 40 % and 66 % of the variance of the scalar IM can be explained by the secondary IM in $\langle S_{a,GM}, N_p \rangle$ in the case of 6- and 9-storey structures, respectively. These values are reduced to 20 % and 50 % for the 6- and 9-storey buildings when near-field ground-motion pairs are considered (Table 6). The benefits of employing the vector $\langle S_{a,GM}, N_p \rangle$ are also evident from Figure 11 where steeper curves are associated with the vector formulation in comparison with the scalar case. Furthermore, this figure also exemplifies the improved ability of this ground-motion parameter to explain the response of the taller 9-storey structures in comparison with the 6-storey ones. The stronger performance of N_p for 9-storey buildings may indicate that the variability in the response of these structures is associated with their non-linear response to a greater degree than for 6-storey structures.

6.2. Drift hazard curves

Figure 12 presents a typical comparison of the drift hazard curves obtained by means of the scalar ($IM = S_{a,GM}(T_1)$) and vector ($\langle IM_1, IM_2 \rangle = \langle S_{a,GM}(T_1), N_p \rangle$) models as outlined in Section 5. Results are presented for far-field and near-field record sets. It is evident from this figure that by considering the shape factor parameter, N_p, as a secondary IM a higher proportion of the structural response is explained, leading to lower drift exceedance rates, especially at larger peak drift levels ($\theta_{max} > 0.02$). For example, the consideration of the vector $\langle S_{a,GM}(T_1), N_p \rangle$ reduces the hazard in about 50% for $\theta_{max} = 0.05$. It is also evident from Figure 12 that the effects of a reduced dispersion brought about by the secondary IM are larger for far-field than for near-field records. However, it should be noted that the higher drift hazards associated with near-field events are a direct result of the larger MRD of the closer seismic source assumed, as described in the previous section.

7. Response comparison of alternative framing systems

From the results presented in previous sections, and summarized in Tables 3 to 6, it cam be observed that different responses are obtained for 6-storey and 9-storey buildings In the case of 6-storey structures, consistently higher capacities (i.e. μ_{lnIM} around 5 % higher) are observed for two-way framing systems at all θ_{max} limits for both near-field and far-field records. Conversely, 5 % lower mean capacities are associated with two-way frames in 9-storey buildings. These trends hold for both near-field non-pulselike as well as far-field ground-motions. These differences can be attributed to the relative importance of second order effects in taller structures coupled with the susceptibility of two-way frames to form plastic hinges almost simultaneously in all its lateral resisting elements. In comparison, due to their inherent flexibility, the gravity frames present in one-way structures will not experience plastic demands up to large levels of θ_{max} making one-way systems relatively more resilient to the effects of increased second-order forces [3].

A number of studies have dealt with the effects of a adequate modelling of gravity frames in steel structures [50, 51, 52, 53] and there is a consensus on the higher collapse capacities brought about by the consideration of the additional stiffness and strength of gravity systems and connection as well as the benefits of a continuous secondary frame in mitigating the concentration

of plastic deformation in a single storey. However, these improved responses have generally been found with reference to 2D models and for θ_{max} values well above 2 %. By contrast, it is evident from the results presented in Tables 3 and 4 that, specially for taller buildings, the benefits of a continuous gravity frame system in enhancing the median building capacities extend to drift levels as low as $\theta_{max} = 0.007$ and hold for both near-field and far-field records. These differences are attributed to the effects of the spatial distribution of strength, stiffness and spectral response in one-way systems that can only be captured through a 3D modelling approach.

Finally, in terms of dispersion (i.e. σ_{lnIM}), significantly lower dispersions are observed for the 6-storey two-way frame in comparison with its one-way counterpart for $\theta_{max} = 0.007$ under both near-field and far-field accelerograms. For all other drift limits, the use of two-way frames is associated with relatively higher σ_{lnIM} values. Similarly, although comparable values of dispersion are evident for one-way and two-way 9-storey structures at $\theta_{max} = 0.007$ and $\theta_{max} = 0.025$, for $\theta_{max} = 0.05$ a significantly larger variability is evident in the response of two-way buildings (e.g. over 10 % higher σ_{lnIM} values at $\theta_{max} = 0.05$). It is important to note that for a given median capacity value (i.e. μ_{lnIM}), an increase in the dispersion (i.e. higher σ_{lnIM}) results in a higher probability $P(EDP > x)$ for values of $S_{a,GM}(T_1)$ lower than the median and a lower probability of exceedance associated with larger $S_{a,GM}(T_1)$ values. This has important implications on the calculation of $\lambda(EDP > x)$ as observed by Eads et al. [54] for scalar approaches. If the results of the fragility function are integrated in accordance with Equation 1, higher values of $P(EDP > x)$ for low $S_{a,GM}(T_1)$ values will be coupled with high hazard levels, thus resulting in an increased overall $\lambda(EDP > x)$. The same phenomenon is observed here for vector-valued formulations (Equation 2). This lays behind the higher likelihood of exceeding given EDP levels observed in 6-storey two-way structures which have otherwise greater median capacities than their one-way counterparts and highlights the importance of an accurate quantification of the dispersions in the structural response.

A direct comparison of the effects of alternative framing configurations, including the positive reductions in the dispersion σ_{lnIM} introduced by the vector approach, can be established with reference to the drift hazard curves depicted in Figure 13. To this end, Figures 13a and 13b present a comparative assessment of structures with one-way and two-way framing systems un-

der far-field and non-pulselike near-field ground-motions, respectively. These curves have been obtained following the procedure outlined in the previous section. It can be appreciated from these figures that the responses of 6- and 9-storey structures follow clear and differentiated trends with higher hazards associated with 6-storey buildings regardless of the ground-motion type. Also, it is evident from Figure 13 that one-way buildings experience consistently lower drift exceedance rates, especially for drift levels larger than 2 %. The smaller drift hazards experienced by one-way systems relative to two-way frames are more evident for the taller 9-storey structures and become more significant as the drift demand level increases. These results align well with those reported by Tawaga et al. [1] for a couple of 3-storey structures subjected to single-component ground-motions who ascribed higher drift exceedance rates to the two-way layout at drifts larger than 3 %. The lower variability and slightly higher relative capacities associated with one-way frames at larger drifts together with the presence of gravity frames that are able to mitigate the second-order effects in taller structures while at the same time reducing the concentration of plastic deformations explain the behavioural trends reported herein.

8. Conclusions

This paper has examined the response of one-way and two-way steel framing systems under bi-directional seismic action with reference to 6- and 9-storey buildings. Far-field as well as near-field non-pulselike earthquake records have been considered. The following findings can be offered in relation to the relative seismic performance of one-way and two-way building configurations:

- Different tendencies are observed for the fragilities of two-way and one-way framing systems depending on the number of storeys. In the case of 6-storey structures, consistently higher capacities are observed for two-way layouts at all peak drift limits for both near-field and far-field records. Conversely, 5 % lower mean capacities are obtained for two-way frames in 9-storey buildings. These differences can be attributed to the increased effect of second order actions in taller structures coupled with the susceptibility of two-way frames to the simultaneous formation of plastic hinges in all its lateral resisting elements.

- By assuming simplified (single-point source) seismic hazard, higher drift hazards are obtained for 6-storey buildings in comparison with their 9-storey counterparts regardless of the ground-motion type or framing system adopted.

- One-way framing systems experience consistently lower drift exceedance rates than two-way frames for drift demands of $\theta_{max} > 0.02$. These differences between the drift hazards of one-way and two-way buildings are more evident for 9-storey structures and become more significant as the deformation demands increase. These trends are attributed to the lower variability on the response of one-way buildings coupled with the presence of gravity frames that help to reduce the concentration of plastic deformations and mitigate second-order effects which will be higher in 9-storey than in 6-storey structures. The stronger performance of the ground-motion shape parameter, N_p, for 9-storey buildings also points towards a greater influence of plastic deformation patters in the response of these structures.

In addition, the following conclusions can be drawn regarding the use of vector-based assessment for bi-directionally loaded structures:

- Linear regression was found to produce more consistent and realistic vector fragility forms for the cases of the bi-directionally excited 3D buildings studied herein.

- The inclusion of the spectral shape parameter, N_p, calculated herein from the geometric mean spectrum of the two horizontal components, significantly reduces the dispersion in the estimation of drift demands of bi-directionally loaded buildings at large deformation levels. As the efficiency of the spectral acceleration, $S_{a,GM}$, decreases with increasing levels of non-linear response, the benefits of including a spectral shape ground-motion parameter like N_p, which accounts for longer periods, become increasingly more evident.

- The improvements on the fragility estimations at larger peak drifts (i.e. $\theta_{max} = 0.02$) induced by the consideration of N_p as a secondary IM are evident irrespective of the framing system under consideration or the nature of the ground-motion set employed (i.e. far-field or non-pulselike near-field). Such improvements were quantified in this study.

Reductions of up to 40 % were observed in the associated standard deviation when the vector $\langle S_{a,GM}, N_p \rangle$ was considered in comparison to a purely scalar formulation for both one-way and two-way buildings subjected to far-field acceleration series.

- Around 40 % and 66 % of the variance of the scalar IM can be explained by the secondary IM in $\langle S_{a,GM}, N_p \rangle$ in the case of 6- and 9-storey 3D structures, respectively, subjected to far-field acceleration pairs. These values are reduced to 20 % and 50 % for the 6- and 9-storey buildings when near-field ground-motion pairs are considered. These improved explanations of the bi-directional structural response brought about by a vector-IM analysis translates into correspondingly lower rates of drift limits exceedance at higher performance levels.

- At lower drift levels (e.g. $\theta_{max} = 0.007$), the spectral ratio, R_{T_3,T_1}, produces statistically significant enhancements in the estimation of the response for all the structures considered under far-field records. The associated reductions in standard deviation are in the order of 10 % with respect to scalar formulations. Similarly, approximately 25 % of the variance of the scalar IM can be explained by R_{T_3,T_1} acting as secondary IM. In contrast, when near-field responses are considered, the inclusion of R_{T_3,T_1} as secondary IM seems to bring limited benefits for all 3D building configurations examined.

- The improvements associated with the implementation of a full vector model are larger when far-field records are considered with respect to non-pulselike far-field ground-motions.

This study constitutes the first attempt to implement a vector-based comparison of the response of the most common steel framing configurations currently employed under realistic bi-directional earthquake action. The results presented in this paper constitute an important step towards discerning the steel framing layout with the most favourable seismic performance at different deformation demand levels while the methods employed provide a comprehensive platform to be used by earthquake engineers in future comparative studies. Although the tendencies documented above are expected to hold for more irregular structures, further work is needed on this topic. This explorations should include the incorporation of the non-stationary characteristics of the ground-motion alongside the frequency related parameters employed

herein in the formulation of IM vectors. All these are matters of on-going and future research.

References

[1] Tagawa H., MacRae G., Lowes L. 2008. Probabilistic evaluation of seismic performance of 3-story 3D one- and two-way steel moment-frame structures. *Earthquake Engineering and Structural Dynamics*, 37, 681-696.

[2] Kiggins S., Uang C.M. 2006. Reducing residual drift of buckling restrained braced frames as dual systems. *Engineering Structures*, 28, 1525-1532.

[3] Málaga-Chuquitaype C., Elghazouli A.Y., Enache R. 2016. Contribution of secondary frames to the mitigation of collapse in steel buildings subjected to extreme loads. *Structure and Infrastructure Engineering*, 12, 45-60.

[4] Marusic D., Fajfar P. 2005. On the inelastic seismic response of asymmetric buildings under bi-axial excitation. *Earthquake Engineering and Structural Dynamics*, 34, 943-963.

[5] Lee C.S., Hong C.S. 2010. Statistics of inelastic responses of hysteretic systems under bi-directional seismic actions. *Engineeering Structures*, 32, 2074-2086.

[6] Chopra A.K., Goel R.K. 1991. Evaluation of torsional provisions in seismic codes. *Journal of Structural Engineering, American Society of Civil Engineers*, 117, 3783-3803.

[7] De Stefano M., Faella C., Ramasco R. 1998. Inelastic seismic response of one-way plan-asymmetric systems under bi-directional ground motions. *Earthquake Engineering and Structural Dynamics*, 27, 363-376.

[8] Chopra A.K., Goel R.K. 2004. A modal pushover analysis procedure to estimate seismic demands for unsymmetric plan buildings. *Earthquake Engineering and Structural Dynamics*, 33, 903-927.

[9] Lin J.L., Tsai K.C. 2008. Seismic analysis of two-way asymmetric building systems under bi-directional seismic ground motions. *Earthquake Engineering and Structural Dynamics*, 37, 305-328.

[10] Liao K.W., Wen Y.K., Foutch D.A. 2007. Evaluation of 3d steel moment frames under earthquake excitations: 1: Modeling. *Journal of Structural Engineering, American Society of Civil Engineers*, 133, 462-470.

[11] Erduran E., Ryan K.L. 2011. Effects of torsion on the behavior of peripheral steel-braced frame systems. *Earthquake Engineering and Structural Dynamics*, 40, 491-507.

[12] Cornell C.A., Jalayer F., Hamburger R.O., Foutch D.A. 2002. Probabilistic Basis for 2000 SAC Federal Emergency Management Agency Steel Moment Frame Guidelines. *Journal of Structural Engineering*, 128, 526-533.

[13] Bazzurro P. 1998. Probabilistic seismic demand analysis. Ph.D. Dissertation, Stanford University, CA, US.

[14] Gehl P., Seyedi D., Douglas J. 2013. Vector-valued fragility functions for seismic risk evaluation. *Bulletin of Earthquake Engineering*, 11, 365-384.

[15] Luco N., Cornell C.A. 2007. Structure-specific scalar intensity measures for near-source and ordinary earthquake ground motions. *Earthquake Spectra*, 23, 357-392.

[16] Faggella M., Barbosa A.R., Conte J.P., Spacone E., Restrepo J.I. 2013. Probabilistic seismic response analysis of a 3-D reinforced concrete building. *Structural Safety*, 44, 11-27.

[17] Málaga-Chuquitaype C. 2011. Seismic design and assessment of steel structures incorporating tubular members. Ph.D. Thesis, Imperial College London, UK.

[18] Spanos C. 2013. Dynamic response of alternative steel framing systems. MEng Thesis, Imperial College London, UK.

[19] Nakashima M., Ogawa K., Inoue K. 2002. Generic frame model for simulation of earthquake responses of steel moment frames. *Earthquake Engineering and Structural Dynamics*, 31, 671-692.

[20] Luco N., Mori Y., Funahashi Y., Cornell A.C., Nakashima M. 2003. Evaluation of predictors of non-linear seismic demands using 'fishbone' models of SMRF buildings. *Earthquake Engineering and Structural Dynamics*, 32, 2267-2288.

[21] McKenna F., Fenves G.L., Scott Micheal. 2000. Open System for Earthquake Engineering Simulation, Pacific Earthquake Engineering Research Center, University of California at Berkeley, CA, US.

[22] Karavasilis T.L., Makris N., Bazeos N., Beskos D.E. 2010. Dimensional response analysis of multistory regular steel MRF subjected to pulselike earthquake ground motions. *Journal of Structural Engineering*, 136 (8), 921-932.

[23] Kumar M., Stafford P.J., Elghazouli A.Y. 2013. Seismic shear demands in multi-storey steel frames designed to Eurocode 8. *Engineering Structures*, 52, 69-87

[24] Málaga-Chuquitaype C., Elghazouli A.Y., Bento R. 2009. Rigid-plastic models for the seismic design and assessment of steel framed structures. *Earthquake Engineering and Structural Dynamics*, 38, 1609-1630.

[25] Foyouzat M.A., Estekanchi H.E. 2016. Application of rigid-perfectly plastic spectra in improved seismic response assessment by Endurance Time method. *Engineering Structures*, 111, 24-35.

[26] Federal Emergency Management Administration. 2009. Quantification of building seismic performance factors, Technical Report, FEMA P695

[27] Ancheta T.D., Darragh R.B., Stewart J.P., Seyhan E., Silva W.J., Chiou B., Wooddell K.E., Graves R.W., Kottke A.R., Boore D.M. 2014. NGA-West2 database, *Earthquake Spectra*, 30, 989-1005.

[28] Beyer K., Bommer J.J. 2007. Selection and Scaling of Real Accelerograms for Bi-Directional Loading: A Review of Current Practice and Code Provisions. *Journal of Earthquake Engineering*, 11, 13-45.

[29] Vamvatsikos D., Cornell C.A. 2002. Incremental dynamic analysis. *Earthquake Engineering and Structural Dynamics*, 31, 491-514.

[30] Vamvatsikos D., Cornell C.A. 2002. Applied incremental dynamic analysis. *Earthquake Spectra*, 20, 523-553.

[31] Baker J.W., Cornell CA. 2006. Which Spectral Acceleration Are You Using? *Earthquake Spectra*, 22, 293-312.

[32] Modica A., Stafford P.J. 2014. Vector fragility surfaces for reinforced concrete frames in Europe. *Bulletin of Earthquake Engineering*, 12, 1725-1753.

[33] Bojórquez E., Iervolino I. 2011. Spectral shape proxies and nonlinear structural response. *Soil Dynamics and Earthquake Engineering*, 31, 996-1008.

[34] Rathje E.M., Faraj F., Russell S., Bray J.D. 2004. Empirical Relationships for Frequency Content Parameters of Earthquake Ground Motions. *Earthquake Spectra*, 20,119-144.

[35] Málaga-Chuquitaype C., Elghazouli A.Y. 2012. Inelastic displacement demands in steel structures and their relationship with earthquake frequency content parameters. *Earthquake Engineering and Structural Dynamics*, 41, 831-852.

[36] Málaga-Chuquitaype C. 2015. Estimation of peak displacements in steel structures through dimensional analysis and the efficiency of alternative ground-motion time and length scales. *Engineering Structures*, 101, 264-278.

[37] Rathje E.M., Abrahamson N.A., Bray J.D. 1998. Simplified Frequency Content Estimates of Earthquake Ground Motions. *Journal of Geotechnical and Geoenvironmental Engineering*, 124, 150-159.

[38] Shinozuka M., Feng M.Q., Lee J., Naganuma T. 2000. Statistical Analysis of Fragility Curves. *Journal of Engineering Mechanics*, 126, 1224-1231.

[39] Baker J.W. 2007. Probabilistic structural response assessment using vector-valued intensity measures. *Earthquake Engineering and Structural Dynamics*, 36, 1861-1883.

[40] Baker J.W. 2015. Efficient Analytical Fragility Function Fitting Using Dynamic Structural Analysis. *Earthquake Spectra*, 31, 579-599.

[41] Shome N., Cornell C.A. 2000. Structural Seismic Demand Analysis: Consideration of Collapse, *in Proceedings* 8th ACSE Specialty Conference on Probabilistic Mechanics and Structural Reliability, 1-7.

[42] Bojórquez E., Iervolino I., Reyes-Salazar A., Ruiz S.E. 2012. Comparing vector-valued intensity measures for fragility analysis of steel frames in the case of narrow-band ground motions. *Engineering Structures*, 45, 472-480.

[43] Agresti A. 2007. An introduction to categorical data analysis. Wiley-Interscience, Hoboken, NJ, US.

[44] Tothong P., Cornell C.A. 2007. Probabilistic Seismic Demand Analysis Using Advanced Ground Motion Intensity Measures, Attenuation Relationships, and Near-Fault Effects. Pacific Earthquake Engineering Research Center, Report PEER 2006/11. CA, US.

[45] Boore D.M., Atkinson G.M. 2008. Ground-motion prediction equations for the average horizontal component of PGA, PGV, and 5 %-damped PSA at spectral periods between 0.01 s and 10.0 s. *Earthquake Spectra*, 24, 99-138.

[46] Baker J.W., Cornell C.A. 2006. Spectral shape, epsilon and record selection. *Earthquake Engineering and Structural Dynamics*, 35, 1077-1095.

[47] Inoue T., Cornell C.A. 1990. Seismic hazard analysis of multi-degree-of-freedom structures. Reliability of marine structures, RMS-8. Stanford, CA, US.

[48] Baker J.W., Jayaram,N. 2008. Correlation of Spectral Acceleration Values from NGA Ground Motion Models. *Earthquake Spectra*, 24, 299-317.

[49] Baker J.W., Cornell C.A. 2006. Correlation of Response Spectral Values for Multicomponent Ground Motions. *Bulletin of the Seismological Society of America*, 96, 215-227.

[50] Reyes-Salazar A., Bojórquez E., Haldar A., Lopez-Barraza A., Rivera-Salas, J. 2014. Seismic Response of 3D Steel Buildings considering the

Effect of PR Connections and Gravity Frames. *The Scientific World Journal*, Article ID 346156, 1-13.

[51] Flores F.X., Charney, F.A., Lopez-Garcia D. 2014. Influence of the gravity framing system on the collapse performance of special steel moment frames. *Journal of Constructional Steel Research*, 101, 351-362.

[52] Shen J., Rou W., Akbas B., Seker O., Uckan E. 2015. Near-collapse behavior of steel buildings with non-ductile concentrically braced frames. *Journal of Constructional Steel Research* , 113, 101-114.

[53] Ruiz-Garcia J., Aguilar J.D. 2015. Aftershock seismic assessment taking into account post-mainshock residual drifts. *Earthquake Engineering and Structural Dynamics* , 44, 1391-1407.

[54] Eads L., Miranda E., Krawinkler H., Lignos D.G. 2013. An efficient method for estimating the collapse risk of structures in seismic regions. *Earthquake Engineering and Structural Dynamics*, 42. 25-41.

Tables

Table 1: Structural characteristics of the 3D frames considered in this study

Frame ID	Number of storeys	Structural system	T_1 (s)	V_y/W_{tot}
6-1W	6	one-way	1.18	0.29
6-2W	6	two-way	1.14	0.31
9-1W	9	one-way	1.43	0.23
9-2W	9	two-way	1.44	0.25

Table 2: Ground motion record summary. Adapted from [26].

ID No.	Rec. Seq. N.	Event name	Recording Station	M_w	α ($^\circ$)	PGA (g)
Far-field records						
1	125	Friuli, Italy	Tolmezzo	6.5	293.30	0.36
2	169	Imperial Valley	Delta	6.5	326.09	0.27
3	174	Imperial Valley	El Centro Array #11	6.5	45.715	0.38
4	721	Superstition Hills	El Centro Imp. Co.	6.5	328.82	0.28
5	725	Superstition Hills	Poe Road (temp)	6.5	227.65	0.34
6	752	Loma Prieta	Capitola	6.9	35.115	0.45
7	767	Loma Prieta	Gilroy Array #3	6.9	100.26	0.44
8	848	Landers	Coolwater	7.3	196.88	0.30
9	953	Northridge	Beverly Hills - Mulhol	6.7	344.70	0.43
10	960	Northridge	Canyon Country-WLC	6.7	347.36	0.41
11	1111	Kobe, Japan	Nishi-Akashi	6.9	56.741	0.37
12	1158	Kocaeli, Turkey	Duzce	7.5	349.41	0.33
13	1244	Chi-Chi, Taiwan	CHY101	7.6	344.58	0.39
14	1485	Chi-Chi, Taiwan	TCU045	7.6	174.74	0.49
15	1602	Duzce, Turkey	Bolu	7.1	288.10	0.76
16	1633	Manjil, Iran	Abbar	7.4	51.079	0.53
Near-field records. No pulse						
17	126	Gazli, USSR	Karakyr	6.8	151.83	0.70
18	160	Imperial Valley-06	Bonds Corner	6.5	329.66	0.68
19	165	Imperial Valley-06	Chihuahua	6.5	285.19	0.25
20	495	Nahanni, Canada	Site 1	6.8	345.42	1.07
21	496	Nahanni, Canada	Site 2	6.8	236.07	0.41
22	741	Loma Prieta	BRAN	6.9	12.856	0.47
23	753	Loma Prieta	Corralitos	6.9	305.69	0.50
24	825	Cape Mendocino	Cape Mendocino	7.0	336.24	1.43
25	1004	Northridge-01	LA - Sepulveda VA	6.7	244.34	0.78
26	1048	Northridge-01	Northridge - Saticoy	6.7	272.79	0.40
27	1176	Kocaeli, Turkey	Yarimca	7.5	267.53	0.27
28	1504	Chi-Chi, Taiwan	TCU067	7.6	141.20	0.39
29	1517	Chi-Chi, Taiwan	TCU084	7.6	235.97	0.74
30	2114	Denali, Alaska	TAPS Pump Sta. #10	7.6	61.627	0.33

Table 3: Median EDP capacity and dispersion for $IM = S_{a,GM}(T_1)$. Far-field records set.

Building	$\theta_{max} = 0.007$		$\theta_{max} = 0.025$		$\theta_{max} = 0.05$	
	μ_{lnIM} (g)	σ_{lnIM}	μ_{lnIM} (g)	σ_{lnIM}	μ_{lnIM} (g)	σ_{lnIM}
6 storey two-way	0.136	0.111	0.576	0.198	1.243	0.273
6 storey one-way	0.128	0.148	0.548	0.154	1.197	0.255
9 storey two-way	0.117	0.200	0.519	0.195	1.242	0.331
9 storey one-way	0.122	0.196	0.540	0.192	1.295	0.297

Table 4: Median EDP capacity and dispersion for $IM = S_{a,GM}(T_1)$. Near-field records set.

Building	$\theta_{max} = 0.007$		$\theta_{max} = 0.025$		$\theta_{max} = 0.05$	
	μ_{lnIM} (g)	σ_{lnIM}	μ_{lnIM} (g)	σ_{lnIM}	μ_{lnIM} (g)	σ_{lnIM}
6 storey two-way	0.133	0.172	0.608	0.155	1.294	0.271
6 storey one-way	0.124	0.185	0.584	0.164	1.233	0.248
9 storey two-way	0.120	0.161	0.528	0.233	1.175	0.268
9 storey one-way	0.124	0.154	0.550	0.222	1.272	0.272

Table 5: Vector-valued fragilities linear regression summary. Far-field records set.

	$\theta_{max} = 0.007$				$\theta_{max} = 0.025$				$\theta_{max} = 0.05$			
IM	b_1	p	R^2	$\hat{\sigma}_{cap}$	b_1	p	R^2	$\hat{\sigma}_{cap}$	b_1	p	R^2	$\hat{\sigma}_{cap}$
6-storey two-way frame												
R_{T_3,T_1}	-0.14	0.050	0.25	0.099	-0.16	0.256	0.09	0.196	0.07	0.714	0.01	0.281
N_p	0.11	0.374	0.06	0.111	-0.21	0.342	0.06	0.198	-0.67	0.013	0.36	0.225
T_m	0.13	0.187	0.12	0.107	0.14	0.451	0.04	0.201	-0.20	0.420	0.05	0.276
T_o	0.13	0.218	0.11	0.108	0.08	0.685	0.01	0.204	0.04	0.898	0.00	0.283
6-storey one-way frame												
R_{T_3,T_1}	-0.08	0.429	0.05	0.149	-0.10	0.321	0.07	0.154	0.02	0.923	0.00	0.264
N_p	0.20	0.165	0.13	0.142	-0.15	0.321	0.07	0.154	-0.63	0.006	0.43	0.200
T_m	0.08	0.536	0.03	0.151	0.04	0.767	0.01	0.159	-0.14	0.549	0.03	0.260
T_o	0.11	0.448	0.04	0.150	0.05	0.729	0.01	0.159	0.17	0.497	0.03	0.259
9-storey two-way frame												
R_{T_3,T_1}	-0.24	0.024	0.32	0.172	-0.10	0.360	0.06	0.196	-0.03	0.875	0.00	0.342
N_p	0.07	0.662	0.01	0.206	-0.17	0.241	0.10	0.192	-0.75	0.000	0.67	0.198
T_m	0.28	0.106	0.18	0.188	-0.20	0.246	0.09	0.192	-0.34	0.252	0.09	0.326
T_o	0.12	0.566	0.02	0.205	-0.18	0.357	0.06	0.196	-0.02	0.949	0.00	0.342
9-storey one-way frame												
R_{T_3,T_1}	-0.21	0.049	0.25	0.176	-0.09	0.396	0.05	0.193	-0.05	0.791	0.01	0.307
N_p	0.07	0.647	0.02	0.201	-0.19	0.177	0.13	0.185	-0.67	0.000	0.66	0.179
T_m	0.26	0.136	0.15	0.187	-0.17	0.332	0.07	0.191	-0.29	0.282	0.08	0.295
T_o	0.13	0.514	0.03	0.200	-0.12	0.540	0.03	0.195	0.01	0.962	0.00	0.308

Table 6: Vector-valued fragilities linear regression summary. Near-field records set.

	$\theta_{max} = 0.007$				$\theta_{max} = 0.025$				$\theta_{max} = 0.05$			
IM	b_1	p	R^2	$\hat{\sigma}_{cap}$	b_1	p	R^2	$\hat{\sigma}_{cap}$	b_1	p	R^2	$\hat{\sigma}_{cap}$
6-storey two-way frame												
R_{T_3,T_1}	-0.04	0.717	0.01	0.178	0.10	0.277	0.10	0.153	0.16	0.304	0.09	0.270
N_p	0.27	0.295	0.09	0.171	-0.11	0.627	0.02	0.160	-0.65	0.095	0.21	0.250
T_m	0.06	0.542	0.03	0.176	-0.11	0.243	0.11	0.152	-0.20	0.212	0.13	0.264
T_o	0.01	0.880	0.00	0.179	-0.06	0.380	0.06	0.156	-0.06	0.642	0.02	0.280
6-storey one-way frame												
R_{T_3,T_1}	-0.10	0.324	0.08	0.185	0.04	0.668	0.02	0.169	0.10	0.476	0.04	0.253
N_p	0.26	0.287	0.09	0.183	-0.22	0.322	0.08	0.163	-0.57	0.074	0.24	0.225
T_m	0.08	0.486	0.04	0.189	-0.09	0.370	0.07	0.165	-0.19	0.202	0.13	0.241
T_o	0.01	0.870	0.00	0.192	-0.04	0.578	0.03	0.168	-0.06	0.616	0.02	0.255
9-storey two-way frame												
R_{T_3,T_1}	-0.14	0.074	0.24	0.146	-0.02	0.855	0.00	0.242	0.13	0.346	0.07	0.269
N_p	0.41	0.102	0.21	0.149	-0.71	0.046	0.29	0.204	-1.06	0.005	0.49	0.199
T_m	0.06	0.512	0.04	0.165	-0.02	0.905	0.00	0.243	-0.10	0.530	0.03	0.275
T_o	0.05	0.545	0.03	0.165	-0.00	0.966	0.00	0.243	0.03	0.831	0.00	0.279
9-storey one-way frame												
R_{T_3,T_1}	-0.10	0.205	0.13	0.149	-0.02	0.854	0.00	0.231	0.14	0.301	0.09	0.270
N_p	0.34	0.147	0.17	0.146	-0.71	0.025	0.35	0.186	-1.06	0.004	0.52	0.196
T_m	0.03	0.772	0.01	0.159	-0.00	0.980	0.00	0.231	-0.12	0.486	0.04	0.277
T_o	0.03	0.700	0.01	0.159	0.02	0.882	0.00	0.231	0.02	0.849	0.00	0.283

Figures

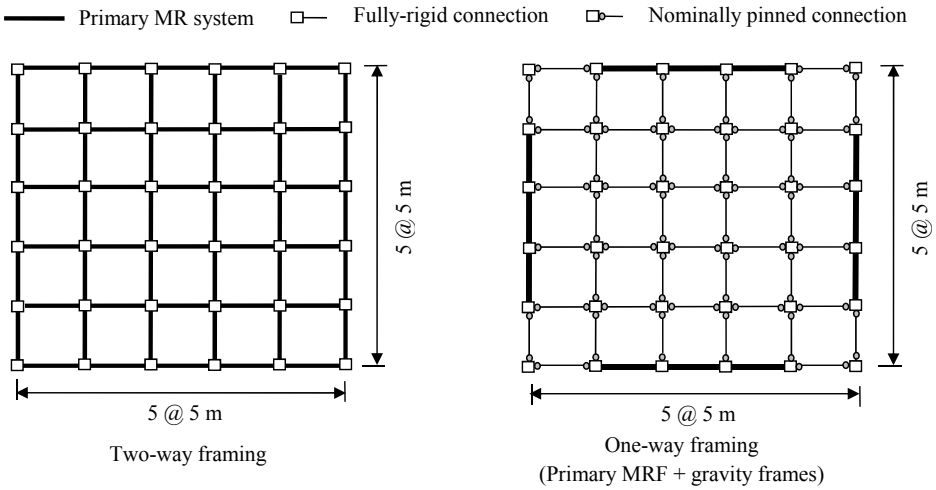

Figure 1: Framing systems plan layout.

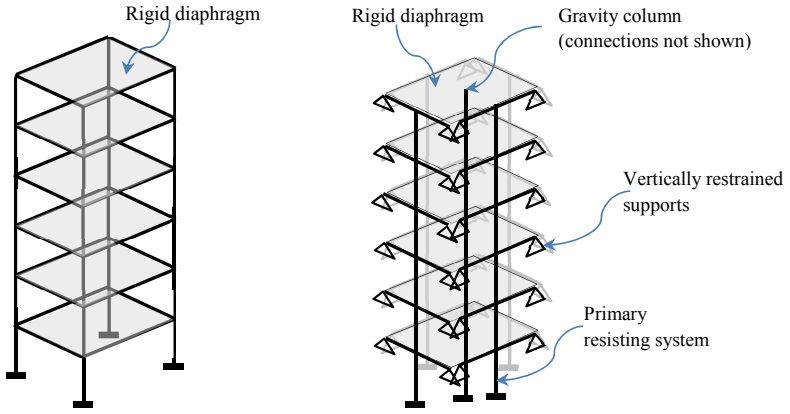

(a) Two-way. (b) One-way.

Figure 2: Schematic view of simplified 3D models.

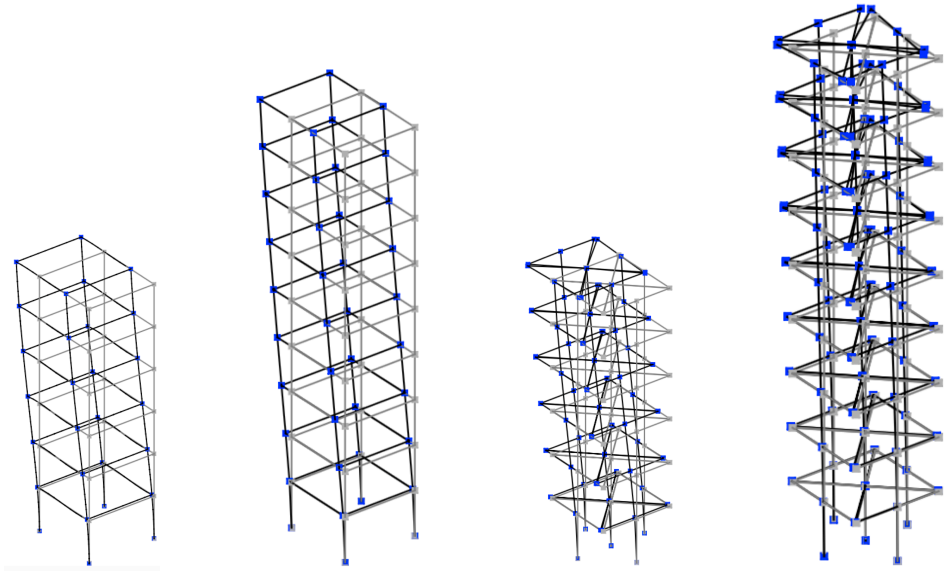

(a) T_1=1.14s. (b) T_1=1.44s. (c) T_1=1.18s. (d) T_1=1.43s.

Figure 3: FE models employed and their fundamental vibration modes: (a) 6-storey two-way, (b) 9-storey two-way, (c) 6-storey one-way, and (d) 9-storey one-way.

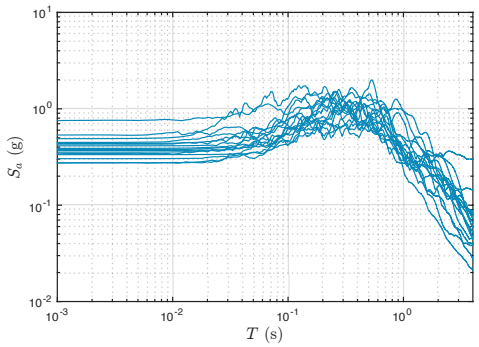

(a) Far field.

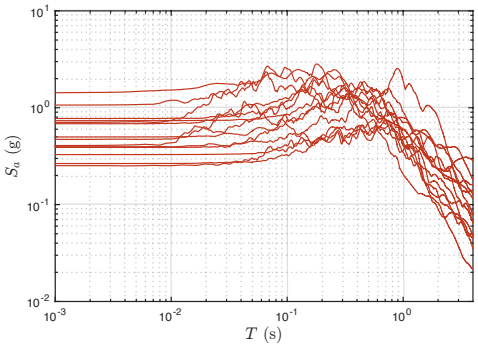

(b) Near field.

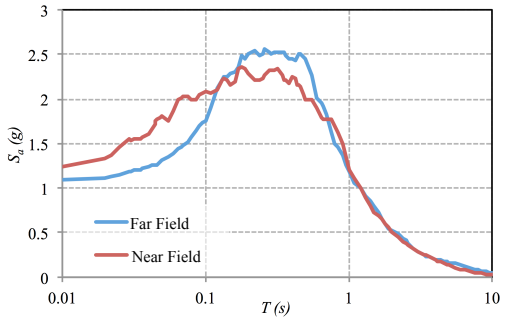

(c) Comparison of median response spectra normalized to $S_{a,GM}(T = 1.2\ s)$

Figure 4: Elastic response spectra of ground-motion records employed. Geometric mean of two horizontal components rotated according to Table 2.

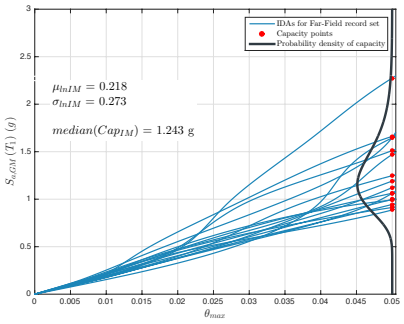

(a) 6-storey two-way frame. Far-field.

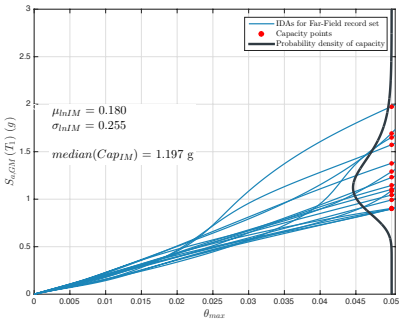

(b) 6-storey one-way frame. Far-field.

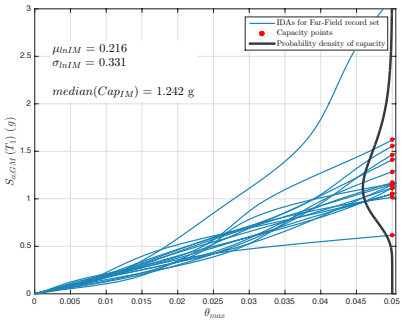

(c) 9-storey two-way frame. Far-field.

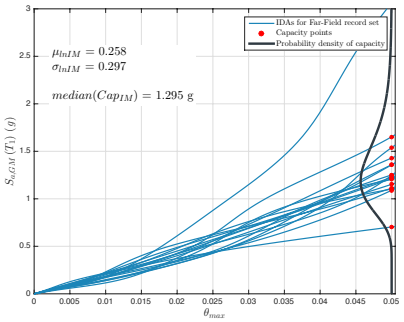

(d) 9-storey one-way frame. Far-field.

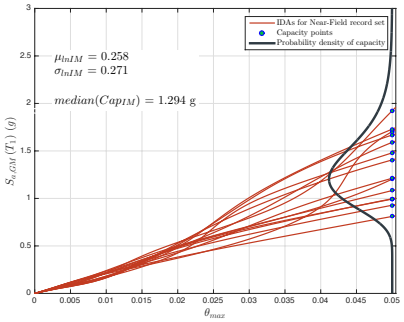

(e) 6-storey two-way frame. Near-field.

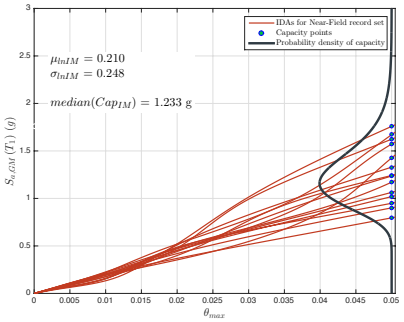

(f) 6-storey one-way frame. Near-field.

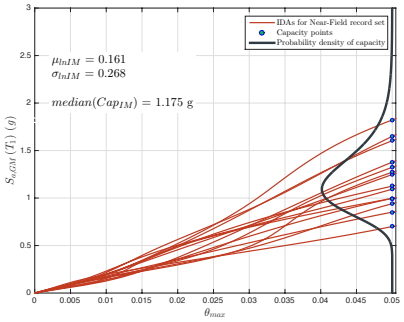

(g) 9-storey two-way frame. Near-field.

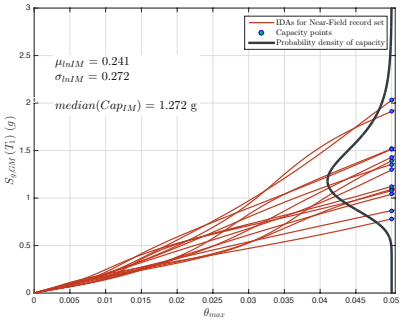

(h) 9-storey one-way frame. Near-field.

Figure 5: IDA curves and fitted log-normal distributions for 5 % peak drift limit.

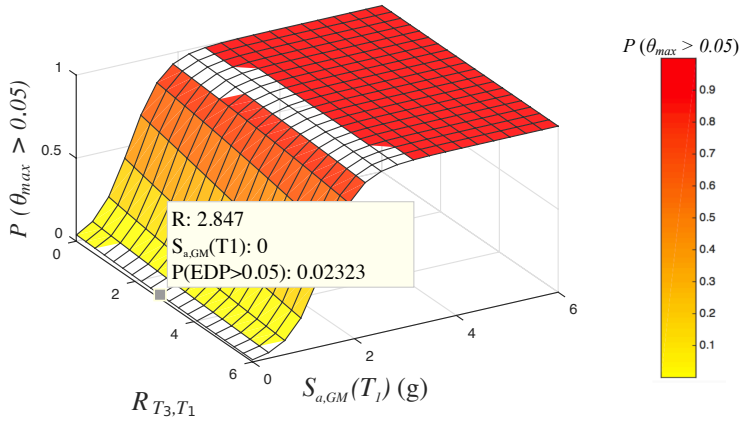

Figure 6: Fragility surface obtained by multiple logistic regression. $\langle IM_1, IM_2 \rangle = \langle S_{a,GM}(T_1), R_{T_3,T_1} \rangle$, 6-storey two-way frame, $\theta_{max} = 0.05$ limit.

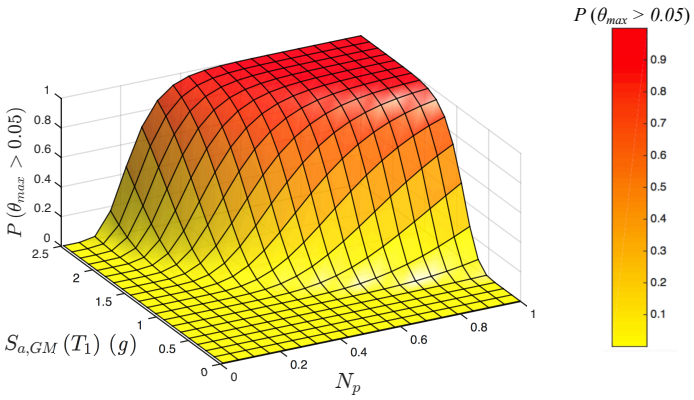

Figure 7: Fragility surface obtained by linear regression. $\langle IM_1, IM_2 \rangle = \langle S_{a,GM}, N_p \rangle$, 6-storey two-way frame, $\theta_{max} = 0.05$ limit.

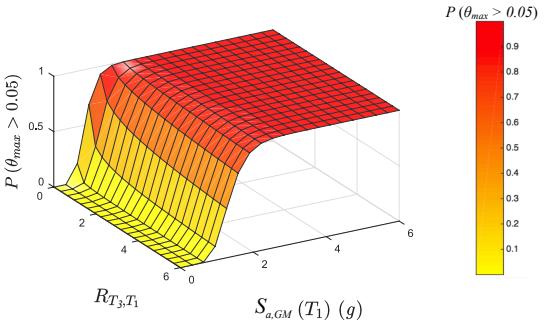

(a) Fragility surface, $\langle S_{a,GM}(T_1), R_{T_3,T_1} \rangle$.

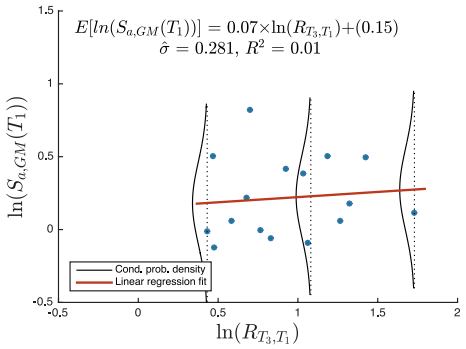

(b) Scatter plot and linear regression fit values, $\langle S_{a,GM}(T_1), R_{T_3,T_1} \rangle$.

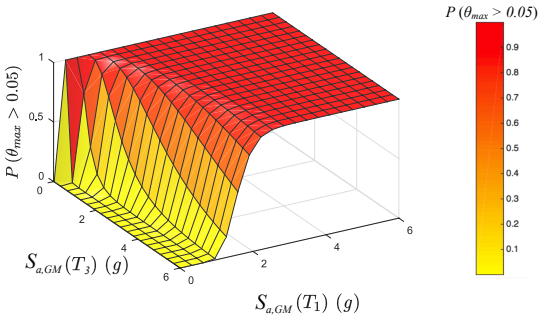

(c) Fragility surface, $\langle S_{a,GM}(T_1), S_{a,GM}(T_3) \rangle$.

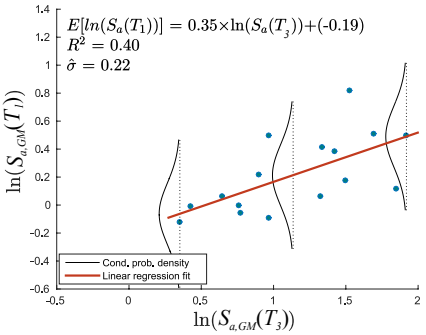

(d) Scatter plot and linear regression fit values, $\langle S_{a,GM}(T_1), S_{a,GM}(T_3) \rangle$.

Figure 8: Linear regression for $\theta_{max} = 0.05$ limit, 6-storey two-way frame. Far-field records.

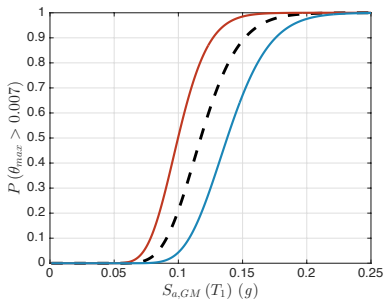

(a) Two-way frame, $\theta = 0.007$.

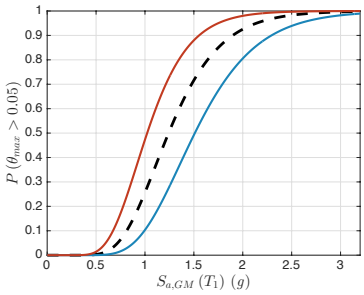

(b) Two-way frame, $\theta = 0.05$.

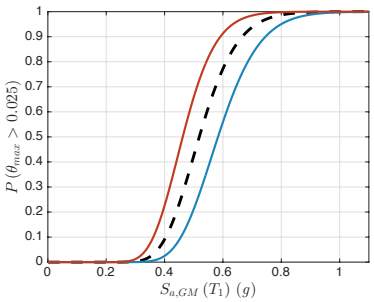

(c) Two-way frame, $\theta = 0.025$.

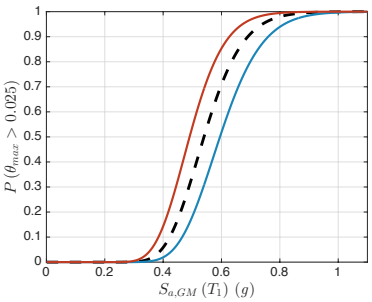

(d) One-way frame, $\theta = 0.025$.

Figure 9: Scalar and vector fragility comparison for far-field records. 9-storey buildings. Dashed black line: scalar $IM = S_{a,GM}$, continuous blue and red lines: $IM = \langle S_{a,GM}, T_m \rangle$ conditional on minimum and maximum value of T_m in the record set.

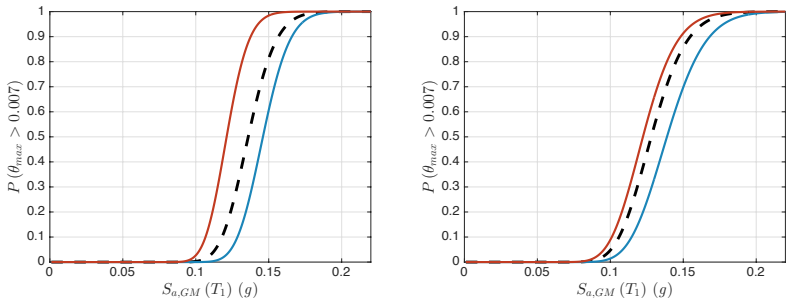

(a) 6-storey two-way frame.

(b) 6-storey one-way frame.

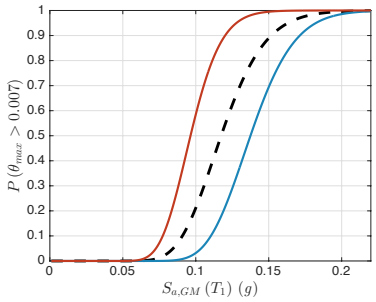

(c) 9-storey two-way frame.

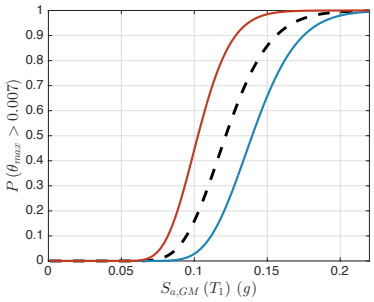

(d) 9-storey one-way frame.

Figure 10: Scalar and vector fragility comparison for $\theta = 0.007$ peak drift limit and far-field records set. Dashed black line: scalar $IM = S_{a,GM}$, continuous blue and red lines: $IM = \langle S_{a,GM}, R_{T_3,T_1} \rangle$ conditional on minimum and maximum value of R_{T_3,T_1} in the record set.

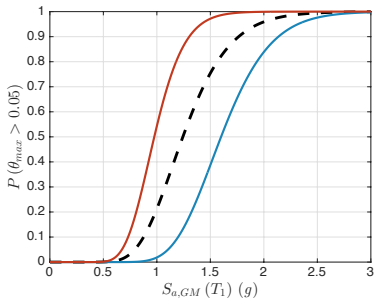

(a) 6-storey two-way frame.

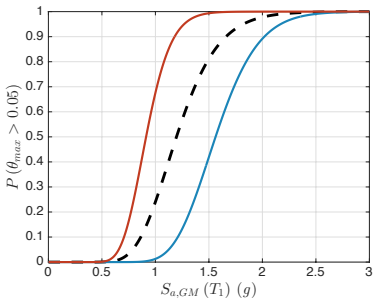

(b) 6-storey one-way frame.

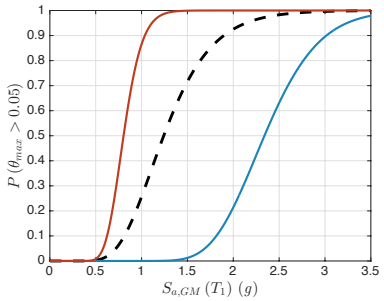

(c) 9-storey two-way frame.

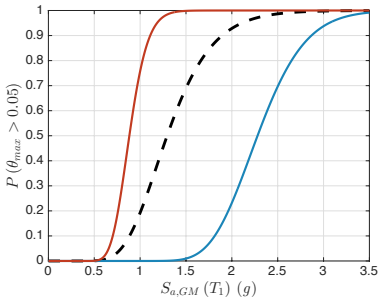

(d) 9-storey one-way frame.

Figure 11: Scalar and vector fragility comparison for $\theta = 0.05$ peak drift limit and far-field records set. Dashed black line: scalar $IM = S_{a,GM}$, continuous blue and red lines: $IM = \langle S_{a,GM}, N_p \rangle$ conditional on minimum and maximum value of N_p in the record set.

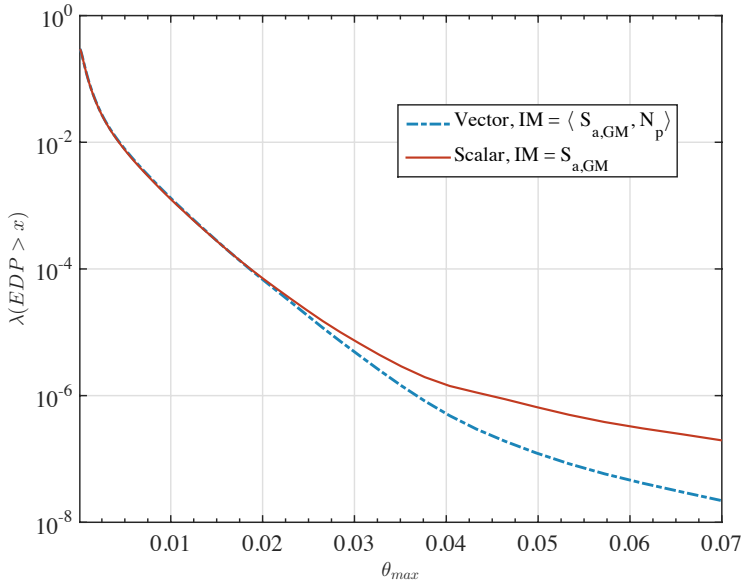

(a) Far-field records set

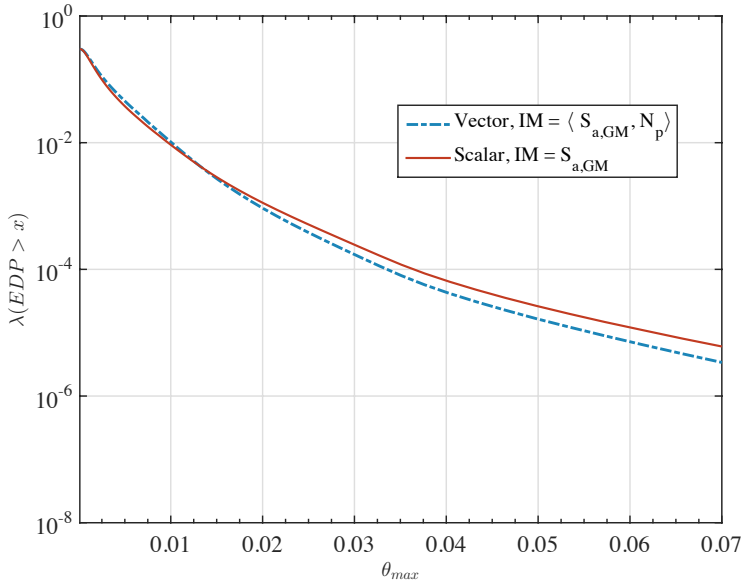

(b) Near-field records set

Figure 12: Comparison of drift hazard curves obtained with scalar and vector IM. 9-storey two-way frame.

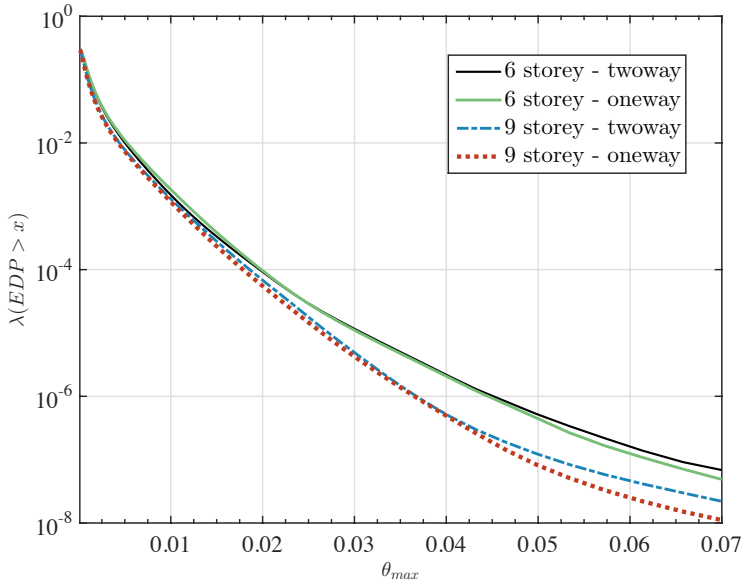

(a) Far-field records set

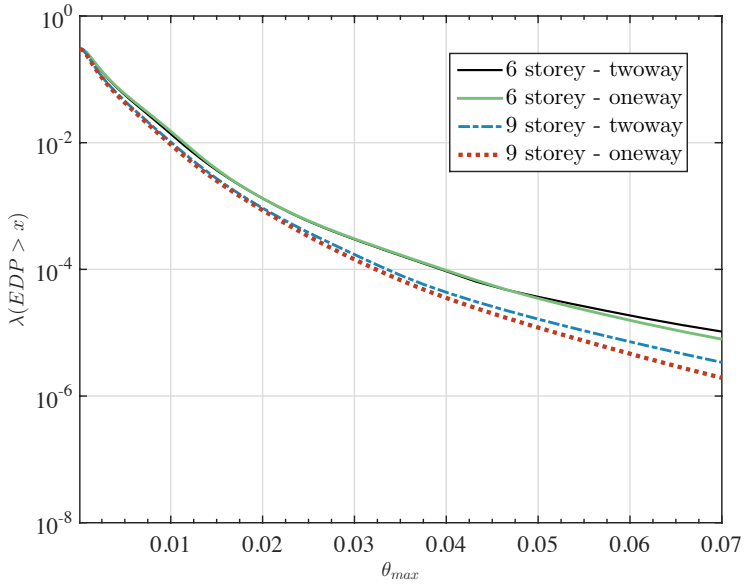

(b) Near-field records set

Figure 13: Drift hazard curves. $IM = \langle S_{a,GM}, N_p \rangle$.